This paper has been published in Metallurgical and Materials Transactions B, and can be accessed through Springer at https://doi.org/10.1007/s11663-019-01642-9

POROSITY PREDICTION IN A356 WHEEL CASTING

P. Fan[1], S.L. Cockcroft[1], D.M. Maijer[1], L. Yao[1], C. Reilly[2], and A.B. Phillion[3]

[1] Department of Materials Engineering, The University of British Columbia, Vancouver, BC, Canada V6T 1Z4

[2] Cast Analytics Inc., Vancouver, BC, Canada V5Z 2H3

[3] Department of Materials Science and Engineering, McMaster University, Hamilton, ON, Canada L8S 4L8

[*]Corresponding author: pan.fan@alumni.ubc.ca

Abstract

A FLUENT^{TM}-based thermal-fluid-compositional model has been developed and applied to a low-pressure, die-cast, A356 aluminium alloy wheel to explore the effects of macro-segregation of hydrogen and late-stage liquid encapsulation on pore formation during solidification. Based on the evolution of temperature, pressure, and hydrogen concentration in the liquid output from FLUENT, the porosity size distribution has been predicted at a number of locations in a commercially produced wheel using an in-house micro-porosity model. The porosity model incorporates pore nucleation kinetics based on hydrogen supersaturation, and two modes of pore growth: the first, occurring at low solid fractions is based on hydrogen diffusion; and the second, occurring at high solid fractions is based on conservation of volume. Samples from a commercially cast wheel have been analyzed using X-ray micro-tomography to provide basic validation of the micro-porosity model. The predicted results showed that the evolution in pressure has the dominant effect on pore growth, but only under conditions where pores have nucleated prior to late-stage liquid encapsulation. Otherwise, the cooling rate appears to have the dominant effect. The accuracy of the model is discussed in terms of the predicted pore size distribution and number density of pores. Areas for continued development are presented.

Keywords

Porosity Prediction, Numerical Simulation, Wheel Casting, A356 Aluminum Alloy

FLUENT is a trademark of Ansys Inc., Canonsburg, PA, United States

Introduction

It is well known that porosity can act as a stress concentrator and crack initiator in cast components thereby degrading fatigue performance[1]. In the case of cast aluminum alloy wheels, there are two main types of porosity: macro-porosity and micro-porosity; the former often also referred to as shrinkage-based porosity and the latter as hydrogen-based porosity.

Macro-porosity occurs in regions in a casting in which a significant volume of liquid is encapsulated and "cut-off" from the supply of liquid needed to compensate for the volume change associated with the liquid to solid transformation. In the case of wheels, macro-porosity is commonly seen at the junction between the rim and spoke, where several solidification fronts can interact. The size and distribution of the resulting porosity depend on the volume of liquid that is encapsulated. Liquid encapsulation in a casting can be accurately predicted using computer-based heat transfer simulation models providing the models are capable of accurately describing the heat transfer occurring during casting. The accurate prediction of the size range and distribution of the macro-porosity, however, remains a challenge.

In contrast to macro-porosity, micro-porosity refers to pores that are relatively small in scale, usually less than 300 μm [1]. Microporosity occurs either due to inadequate compensatory flow in the mushy zone (semi-solid material) at high fractions of solid and/or the exsolution of gas. In the case of the aluminum alloy castings, it is well known that the solubility of hydrogen in the liquid is much higher than in the solid. Aluminum is prone to picking up hydrogen when held in the liquid state particularly under warm and humid conditions. During solidification, hydrogen is rejected from the solid phase into the adjacent liquid. When the hydrogen concentration, or more specifically, the activity of hydrogen in the liquid exceeds its local solubility plus an additional amount to overcome nucleation, a hydrogen bubble will form. Over the last several decades, there has been a significant body of work presented in the literature to understand, characterize and simulate the formation of hydrogen-based porosity. The reader is referred to a good review of early work by Lee *et al.* [2] and more recent work can be found in [3-8].

One aspect of hydrogen pore formation that has not received much attention is the extent to which its formation is influenced by macro-segregation. Macro-segregation of alloying elements, resulting from the relative motion between the solid and liquid phases, has been extensively studied, however, the effects of macro-segregation on hydrogen transport have not been studied [9-12]. This manuscript presents the results of a comprehensive mathematical simulation of hydrogen macro-segregation and micro-porosity formation in an A356 automotive wheel produced at a commercial facility. The research also involved conducting X-ray micro-tomography (XMT) scans of sections of the wheel in order to characterize the size distribution of porosity for model validation. The results of the simulation are presented and compared to the results of the XMT analysis. The factors affecting pore growth including the importance of macro-segregation of hydrogen are discussed.

The simulation of hydrogen macro-segregation builds on previously published work on the simulation of macro-segregation of silicon in a commercially produced wheel using the commercial Computational Fluid Dynamics (CFD) Package FLUENT^{TM} [12]. The results of the FLUENT^{TM}-based analysis are then input into a hydrogen-based pore nucleation and growth model, first proposed by Yao *et al.*[5]. The updated porosity model contains the input of hydrogen macro-segregation from FLUENT^{TM} analysis and two distinct mechanisms of pore growth dependent on the fraction liquid.

Experimental Methodology

A plant trial was conducted with an instrument production die to obtain data suitable for validation of the thermal-fluid-compositional model. Data were collected from the die using thermocouples (TCs) placed within the die and solidified in the wheel under cyclic stead-state casting conditions. Additionally, samples were removed from the wheel for microstructural examination. The examination included quantification of the area fraction of eutectic (used to estimate the local mass fraction of Si) and the pore content. The details surrounding the validation of the model predictions in terms of the evolution in temperature within the wheel and the macro-segregation of Si are presented in an earlier publication—refer to Reference 12.

In-Die and In-Wheel Temperature Characterization

Briefly, 4 thermocouples were installed at various locations on the external surfaces of the various die sections, two on the top die, one on the bottom die, and on on the side die- see TCs 7 20, 24, and 42 in Figure 1. Additionally, several thermocouples were solidified into the wheel to provide data for verifying the evolution in temperature within the wheel—see locations B, C, and D in Figure 1. All of the thermocouples were type-K and sheathed in stainless steel. 1/8" diameter TCs were used for the in-die measurements and 1/16" diameter TCs were used for the in-wheel measurements. In each case, the tips were exposed to facilitate good contact with the die materials/solidifying aluminum.

The data collected from the wheel (and subsequently confirmed by the model predictions) indicated that solidification with this particular die design begins approximately mid-rim and then proceed simultaneously both up toward the in-board rim flange and down toward the rim/spoke junction and then finally across the spoke, finishing at the top of the sprue.

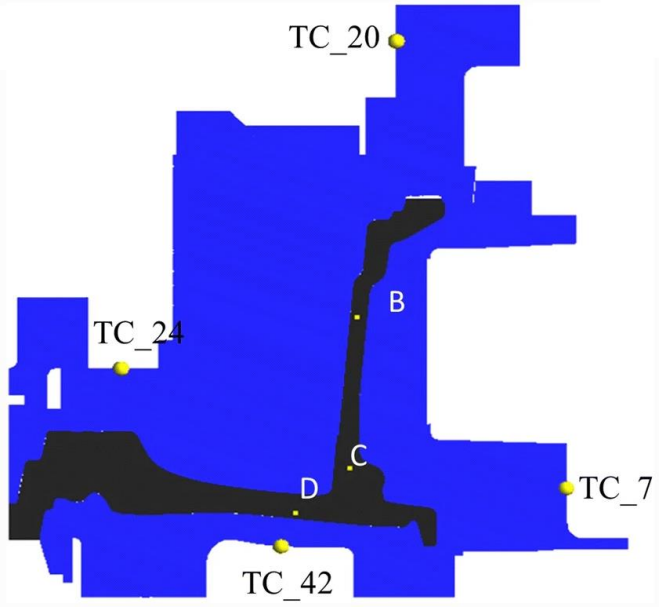

Figure 1: Thermocouple locations in the wheel and die cross-section, cutting plane through wheel spoke

Porosity Characterization

Figure 2(a) shows the location of the ten samples taken from a planar section removed from the rough-machined wheel. Figure 2(b) shows the location of the planar section, together with the names commonly used to describe the various sections of the wheel. To quantify the pore content within the wheel (both number density and pore volume) each of the 10 samples was scanned using X-ray micro-tomography (XMT). The imaging was performed at the Research Complex at Harwell within the Rutherford Appleton Laboratory, Harwell, UK using a Nikon XTH 225 ST system. Figure 2 shows the approximate location of scans and also provides the naming convention used when presenting the results. Two XMT scans were performed on each of the 10 sections to acquire datasets consisting of 2000 slices at voxel resolutions of 5.9, 6.3, or 9.8 μm. As the resolution is dependent on the diameter of a specimen, different resolutions were used for the different sections based on their cross-sectional area. Th scanner settings were set to a source voltage between 80 and 100 kV. 2001 projections scanning 360 deg were recorded.

Figure 2: Location of samples extracted from the wheel for examination (*a*), 36 deg section of the wheel indicating location of section examined (*b*), sample locations and labeling used for X-ray tomography analysis (*c*). Note that pores with sizes less than 20 μm were not analyzed—*i.e.*, pores with less than 27 voxels (3 × 3 × 3 cube), ~ 20 μm in radius

Each XMT image was processed using ImageJ to extract an estimate of the pore size (quantified by measuring the equivalent radius of a spherical pore with the same volume). The pores within a given size ranged were then binned to provide the number density. There were many challenges identified in processing the images. Firstly, a suitable gray-scale threshold to distinguish a pore from metal in the images needed to be identified. After a number of tests, a threshold of 65 was selected – ie a pixel value < 65 is considered as porosity. Secondly, in assessing the pores there is the potential to have a single pore with a complex, tortuous morphology, interpreted as a number of discrete pores. To attempt to address this, the 'Dilate' operation was first applied 10 times, followed by 'erode' 10 times, prior to quantifying the porosity sizes and number densities. This combination of operations combines isolated pores in close proximity to one another into a single pore with a minimal impact on volume to avoid an artificial increase in the estimate of the pore size. The reader is referred to reference 6 for additional details on this methodology.

The effect of above gray-scale threshold and dilate/erode operations are shown in Figures 3(a) and (b), respectively. As can be seen in the series of images shown in Figure 3(a), the threshold value of 65 has preserved what appear to be real pores. The effect of the dilate/erode combination, shown in the series of images in Figure 3(b), can be seen to (1) combine a group of adjacent, isolated pores (likely a single tortuous pore) into a single pore (red circles on the 2D binary image); and (2) retain the original pore size of isolated pores (blue circles on the 2D binary image). Comparing the 3D rendered images, it clearly shows the pore clusters in the green circles are now interpreted as individual pores instead of a group of smaller pores. The experimental data at all locations were obtained by applying a threshold value of 65 and the 'Dilate' and 'Erode' filter combination.

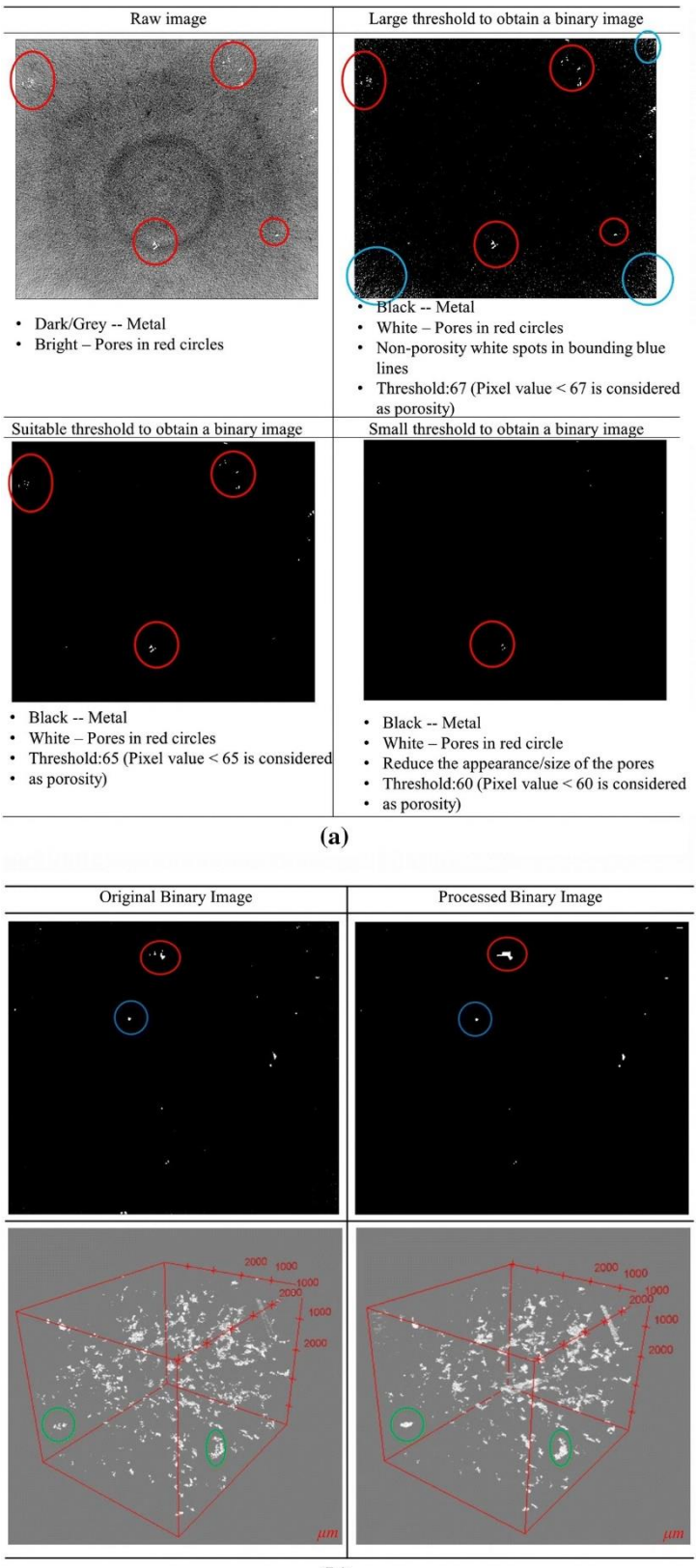

Figure 3: Effect of gray-scale threshold (*a*), and 'Dilate' and 'Erode' filter combination on image processing (*b*)

A coupled thermal-fluid-composition model has been developed using the commercial software package, FLUENT^{TM}, version 16.0, to predict hydrogen macro-segregation during solidification of a LPDC automotive wheel, as well as macro-segregation of the main alloying elements. A detailed description of the model geometry, boundary conditions and material properties are presented in an earlier publication[10]. The model geometry includes the various die components, which are made principally from H13 tool steel, and the wheel, which is an A356 aluminum alloy. The previous publication [10] focused on the application of the model to predict silicon macro-segregation in the wheel. The work included a comparison between the predictions of the model, process thermocouple data and the measured silicon distribution.

In FLUENT^{TM}, the wheel, which undergoes solidification, is treated as a single domain continuum. Significant phenomena during solidification, such as the release of latent heat, the variation in permeability within the two-phase (mushy) region that forms during solidification and the amount of solute rejected from the solid to the liquid (as is the case for normally segregating species) are all formulated as direct functions of the liquid fraction, f_l. The default solidification modelling capabilities within FLUENT^{TM} allow for the prediction of the evolution of f_l for multi-component systems based on data extracted from binary alloy phase diagrams. In the previous work, A356 was treated as an Al-7wt.%Si-0.3wt.%Mg alloy and the relevant data was extracted from the Al-Si and Al-Mg phase diagrams including, the mass fraction of the eutectic, the partition coefficients, the melting point of the pure solvent, the eutectic temperatures and the slope of the liquidus lines. Species conservation within the liquid phase in FLUENT^{TM} includes transport by both diffusion and advection and source and sink terms based on either the Lever Rule or Scheil models as user selected options. Combined, these options allow the evolution of the mass fraction of a given alloy species in the liquid phase and the overall mass fraction to be estimated on an element-by-element base within the computational domain. Unfortunately, the formulation adopted in FLUENT^{TM} does not allow for the tracking of non-alloying species such as hydrogen as many of the parameters needed for input do not exist.

Numerical Model

A coupled thermal-fluid-composition model has been developed using the commercial software package, FLUENT^{TM}, version 16.9, to predict hydrogen macro-segregation during solidification of a low-pressure, die-cast (LPDC) automotive wheel, as well as macro-segregation of the main alloying elements. A detailed description of the model geometry, boundary conditions, and material properties are presented in an earlier publication [12]. The model geometry includes the various die components, which are made principally from H13 tool steel, and the wheel, which is an A356 aluminum alloy. The previous publication focused on validation of the model thermally and the application of the model to predict silicon macro-segregation in the wheel. The work included a comparison between the predications of the model, process thermocouple data, and the measured silicon distribution.

In FLUENT^{TM}, the wheel, which undergoes solidification, is treated as a single domain continuum. Signification phenomena during solidification, such as the release of latent heat, the variation in permeability within the two-phase (mushy) region that forms during solidification, and the amount of solute rejected from the solid to the liquid (as is the case for normally segregating species) are all formulated as direct functions of the liquid fraction, f_l. The default solidification modeling capabilities within FLUENT^{TM} allow for the predication of the evolution

of f_l for multi-component systems based on data extracted from binary alloy phase diagrams. In the previous work, A356 was treated as an Al-7wt pctSi-0.3wt pctMg alloy and the relevant data were extracted from the Al-Si and Al-Mg phase diagrams including the mass fraction of the eutectic, the partition coefficients, the melting point of the solvent, the eutectic temperatures, and the slope liquidus lines. Species conservation within the liquid phase in FLUENT™ includes transport by both diffustion and advection and source and sink terms based on either the Lever Rule of Scheil models as user-selected options. Combined, these options allow the evolution of the mass fraction of a given alloy species in the liquid phase and the overall mass fraction to be estimated on an element-by-element base within the computational domain. Unfortunately, the formulation adopted in FLUENT™ does not allow for the tracking of non-alloying species such as hydrogen as many of the parameters needed for input do not exist.

Hydrogen Conservation

To be able to predict the transport of hydrogen, user-defined scalars (UDS in FLUENT™'s nomenclature) were defined and evaluated as a function of the liquid fraction within a user-defined function (UDF). Two user-defined scalars, UDS_0 and UDS_1, were formulated to represent the mass fraction of hydrogen in the liquid, $C_{H,l}$, and overall mass fraction, C_H. The species conservation for hydrogen in the liquid is given in Eq [1], after Voller [9]:

$$\frac{\partial}{\partial t}(\rho_l UDS_0) = -\nabla\left(\rho_l f_l v_{liq} UDS_0\right) - k_H UDS_0 \frac{\partial}{\partial t}\left(\rho_s(1-f_l)\right) + \frac{\partial}{\partial t}(\rho_s(1-f_l)UDS_0) \qquad \text{Eq [1]}$$

where ρ_l is the liquid density (kg/m^3), f_l is the volume fraction of liquid, ρ_s is the solid density (kg/m^3) and k_H is the segregation coefficient for H. The LHS of Eq [1] represents the evolution of UDS_0 due to the combined effects of the liquid motion and the sink and source terms associated with solidification. The second and third terms on the RHS of Eq [1] are based on the Scheil model to describe hydrogen partitioning between the liquid and solid. Note that Eq [1] omits the term related to the diffusion of hydrogen based on an assessment of the solutal Péclet (~10), where the length scale for assessment was taken to be the size of a computational cell.

Once $C_{H,l}$ is solved through Eq [1], the overall mass fraction of hydrogen (C_H) can be computed from Eq [2] as follows:

$$\frac{\partial}{\partial t}(\rho UDS_1) = \frac{\partial}{\partial t}(\rho_l f_l UDS_0) + k_H UDS_0 \frac{\partial}{\partial t}\left(\rho_s(1-f_l)\right) \qquad \text{Eq [2]}$$

where ρ is the average density (kg/m^3) within a given cell. The average density is calculated via Eq [3] as follows:

$$\rho = \rho_l f_l + \rho_s(1-f_l)$$

Solidification Model and Evolution in Fraction Solid

The material in the wheel domain is A356, which is simplified and treated as Al-7wt%Si-0.3wt%Mg. The liquidus and solidus temperatures ($T_{liquidus}$, $T_{solidus}$) of the alloy are calculated as follows:

$$T_{liquidus} = T_{melt} + \sum_{i=1}^{n} m_i C_{l,i} \qquad \text{Eg [4]}$$

$$T_{solidus} = T_{melt} + \sum_{i=1}^{n} \frac{m_i C_{l,i}}{k_i} \qquad \text{Eq [5]}$$

where T_{melt} is the melting point of pure Al, taken to be 660˚C, m_i (K/wt%) is the slope of the binary alloy liquidus line with respect to species *i*, $C_{l,i}$ is the mass fraction of species *i* in the liquid at a given time increment, k_i is the binary alloy partition coefficient of species *i*, and *n* is the number of alloy additions. $T_{liquidus}$ and $T_{solidus}$ are evaluated in each element within the domain and at each time increment. As these temperatures depend on the local liquid concentration with respect to the main alloy components of *Si* and *Mg*, they are affected by macro-segregation within the casting.

Once the liquid mass fraction of alloy species reaches the "effective" eutectic mass fraction at a given point in the computational domain, FLUENT™ terminates the solution of the species conservations equations. Solidification proceeds to release the heat associated with the latent heat of the phase transformation without further solution of the species conservation equations in FLUENT™. Thus, the liquid mass fractions of Si, Mg and hydrogen are no longer updated for the balance of the solidification process. This makes sense for Si and Mg as the growth of the eutectic will not result in further local liquid enrichment. This is not the case for hydrogen, as hydrogen will continue to be rejected, further enriching the liquid phase in hydrogen, until the melt is fully solidified. The approach to address this is discussed below in the context of the hydrogen pore formation model and the factors affecting pore nucleation and growth.

Pore Nucleation and Growth Model

The pore nucleation and growth model originally developed by Yao *et al.*[5] has been used to predict the evolution in porosity at discrete locations in the wheel casting. As compared with previous applications of this model, the current approach includes several differences: 1) the mass fraction of hydrogen in the liquid (UDS_0 *or* $C_{H,l}$)is input from FLUENT™ taking into account changes in composition due to macro-segregation (previously only microsegregation, based on the Scheil equation, was considered); 2) the evolution of f_l is now input from FLUENT™ to take into account changes in composition due to macro-segregation (previously f_l was based on temperature); and 3) pore growth has been broken into two stages. In terms of the description of pore growth, previously diffusion and pressure-based growth were considered to be active over the entire range of liquid fraction. In the updated approach, pore growth occurs in two stages based on whether mass feeding can occur. In stage I, pore growth is assumed to follow the previous approach[5] where pore growth is controlled by local hydrogen diffusion and pressure. In stage II, pore growth is based on the conservation of volume in small areas of liquid encapsulation once a critical solid fraction is reached, consistent with the end of mass feeding.

A detailed description of the porosity model can be found in [9]. In brief, nucleation within the pore model is assumed to be a function of supersaturation *ss* (mol/m^3) and can be described by a Gaussian function of the form:

$$\frac{dN}{d_{ss}} = \frac{A}{\sqrt{2\pi}\sigma} exp\left(-\frac{(ss-ss_0)^2}{2\sigma^2}\right) \quad \text{Eq [6]}$$

where N (mm^{-3}) is the number density of the nuclei, A (mm^{-3}) represents the total number of available nuclei, σ (mol/m^3) represents the variation in potency of nucleation sites, ss_0 (mol/m^3) represents the average supersaturation for pore nucleation. A, ss_0 and σ are adjustable parameters and associated with the melt properties, such as for example the concentration of oxides in the melt. The solution method involves assigning the pores nucleated within a user-specified supersaturation range to a bin, where N_j would be the number of pores in the j_{th} bin. In this approach,

all of the pores within a given bin are assumed to have the same radius, allowing an evolving distribution of pore sizes to be tracked efficiently.

The supersaturation *ss* (mol/m^3) is defined as the difference between the local molar concentration of hydrogen in the liquid, $C_{H,l}^M$ (mol/m^3), and the molar saturation concentration of hydrogen, $C_{H,sat}^M$ (mol/m^3). The former is incrementally output from FLUENT^{TM} (Eq [1], UDS_0) prior to eutectic transformation and then computed by mass conservation of hydrogen in the liquid via Eq [7] after [9]. *Note: the raw output of UDS_0 from FLUENT^{TM} is mass fraction, which is then converted to molar concentration in the porosity model.*:

$$\Delta f_s \cdot C_{H,l}^M (1 - k_H) \cdot V_{VE} = \Delta\left(f_l \cdot C_{H,l}^M \cdot V_{VE}\right) + \Delta \sum_i \left(\frac{N_j P_g V_g}{RT}\right)_i \quad \text{Eq [7]}$$

where V_{VE} (m^3) is the volume of the computational volume element and k_H is the partition coefficient of hydrogen, T(K) is the temperature and R (J/mol/K) is the ideal gas constant. The LHS of Eq [7] represents the amount of hydrogen rejected from the solid due to an increment in solid fraction, f_s, as estimated based on the Scheil equation, and the RHS of Eq [7] represents the increase in hydrogen concentration in the liquid and the increase in the amount of hydrogen in the pores. The transition in updating $C_{H,l}^M$ from the value output from FLUENT^{TM} to the Scheil approximation at a given point in the computational domain is dependent on the f_l at which the eutectic transformation occurs (f_{eut} - e.g. $C_{H,l}^M$ is based on the output data from FLUENT^{TM} when f_l is above f_{eut} and the Scheil Equation when f_l is less than the f_{eut}).

The molar saturation concentration of hydrogen is calculated via Sievert's Law:

$$C_{H,sat}^M = K_L \sqrt{P_a + P_h + \Delta P_d} \quad \text{Eq [8]}$$

where K_L is the temperature-dependent equilibrium constant (mol/m^3/atm$^{1/2}$) [12], P_a (Pa) is the atmospheric pressure, P_h (Pa) is the metallostatic pressure, and ΔP_d (Pa) is the pressure drop associated with attenuated flow in the mushy zone. The term ΔP_d is also output from FLUENT^{TM}, and is further discussed below in the section related to the Darcy source term. Thus, the nucleation rate is determined by a combination of the characteristics of the melt (number of heterogeneous nucleation sites), the local hydrogen concentration and the local pressure.

In this model, pore growth is divided into two stages. In Stage I, pores grow because of diffusive transfer of hydrogen from the liquid to the pore. The molar transfer rate of hydrogen to the pores within the j^{th} bin can be calculated as [9]:

$$\frac{dn_{H,j}}{dt} = D_{H,liq} \cdot 4\pi r_{p,j}^2 \cdot \varphi \frac{C_{H,l}^M - C_{lp}}{l_{diff}} \quad \text{Eq [9]}$$

where n_H (mol) is the total moles of hydrogen transferred to the pore, $D_{H,liq}$ (m^2/s) is the diffusion coefficient of hydrogen in the liquid, $r_{p,j}$ (m) is the radius of the pores in the j^{th} bin (timestep). φ is the growth impingement factor $(1-f_s)^m$, which accounts for the reduction in pore surface area for mass transfer due to the solid dendritic structure (*the diffusion rate of hyrodgen in the solid is several orders of magnitude lower than in the liquid* [5]) and l_{diff} is the diffusion length in the

liquid, approximated as the pore radius, *i.e.* $l_{diff} = r_p$. The C_{lp} (mol/m^3) represents the equilibrium hydrogen concentration at the liquid/pore interface, given by:

$$C_{lp} = K_L\sqrt{P_a + P_h + \Delta P_d + \frac{2\gamma}{r_p}} \quad \text{Eq [10]}$$

where $\frac{2\gamma}{r_p}$ (Pa) is the pressure exerted by surface tension. The volume of each pore in the j^{th} bin is updated through the ideal gas law as below:

$$\frac{dn_{H,j}}{dt} = \left(\frac{P_{p,j}V_{p,j}}{R_g T}\right)^{t+\Delta t} - \left(\frac{P_{p,j}V_{p,j}}{R_g T}\right)^{t} \quad \text{Eq [11]}$$

where the pressure within a pore is given by Eq [12] and $V_{p,j} = \frac{4\pi}{3} r_{p,j}^3$

$$P_{p,j} = P_a + P_h + \Delta P_d + \frac{2\gamma}{r_{p,j}} \quad \text{Eq [12]}$$

where P_a (Pa) is the ambient pressure, P_h (Pa) is the pressure head within the liquid metal, ΔP_d (Pa) is the pressure drop within the dendritic network and $\frac{2\gamma}{r_{p,j}}$ (Pa) is the pressure associated with pore radius. The approach to calcualte ΔP_d is given below in the next section.

In the current work, the diffusion-based mechanism for pore growth is suspended at a critical solid fraction consistent with the end of inter-dendritic mass feeding. This has been done for two reasons: firstly, at low f_l the rate of diffusion-based growth is reduced significantly by the increasing amount of solid adjacent to a given pore as the impingement factor φ will be nearly zero – refer to Eq [9]; secondly, the CFD code struggles with calculating the reduction in pressure ΔP_d that will occur in the small pockets of interdendritic liquid as they solidify given the size of the volume elements adopted in the domain. Given this limitation, a second mechanism of pore growth, Stage II, has been formulated based solely on the conservation of volume in small volumes of liquid encapsulation. In this approach, once late-stage liquid encapsulation/isolation occurs, the mass conservation (continuity) equation is modified such that solidification shrinkage is compensated by the growth of existing pores (assuming solid deformation can be ignored). Thus, the mass conservation equation is changed in the porosity model to the following expression:

$$\frac{\partial \rho}{dt} = \rho_l \frac{\partial f_p}{\partial t} \quad \text{Eq [13]}$$

where ρ (kg/m^3) is the overall density, ρ_l (kg/m^3) is the density of the liquid, and f_p is the volume fraction of porosity. (*Note: this is done in the porosity model only)*. Assuming $\rho = f_l\rho_l + f_s\rho_s$, Eq [13] can be rewritten as:

$$\frac{\partial f_p}{\partial t} = \frac{\rho_l}{(\rho_s - \rho_l)} \frac{\partial f_s}{\partial t} \quad \text{Eq [14]}$$

The total change in pore volume is then given in Eq [15]:

$$\Delta V_{total,p} = \frac{\rho_l}{(\rho_s - \rho_l)} \frac{\partial f_s}{\partial t} \cdot \Delta t \cdot V_{VE} \cdot \varphi \quad \text{Eq [15]}$$

where V_{VE} (m^3) is the volume of the computational volume element and Δt (s) is the increment in time. The product of $V\varphi$ represents the effective volume that pores can grow into – see also Eq [9]. Assuming the change in volume in each pore is the same, the change in volume per pore is then:

$$\Delta V_p = \frac{\Delta V_{total,p}}{\sum_{j=0}^{m} N_j} \quad \text{Eq [16]}$$

where m is the total number of bins, N_j is the number of pores in the j_{th} bin. Finally, the expression for the change in radius of the pores in the j^{th} bin is then equal to

$$\left(\frac{4\pi}{3} r_{p,j}^3\right)^{t+\Delta t} = \Delta V_p + \left(\frac{4\pi}{3} r_{p,j}^3\right)^{t} \quad \text{Eq [17]}$$

where $r_{p,j}$ (m) is the radius of the pores within the j_{th} bin.

Pressure Drop

In FLUENT™, the semi-solid region (mushy zone) is treated as a porous medium. A momentum sink term, S ($kg/m^2/s^2$), is added to represent the momentum loss as the permeability decreases in the mushy zone with decreasing f_l:

$$S = -\frac{(1-f_l)^2}{(f_l^3+\varepsilon)} A_{mush} v \quad \text{Eq [18]}$$

where ε is a small number (0.001) added to avoid division by zero, v (m/s) is the superficial liquid velocity, equal to the product of liquid fraction and liquid velocity, $v=f_l\overrightarrow{v_l}$. The term A_{mush} ($kg/m^3/s$) is the velocity attenuation parameter; the higher the value, the larger the resistance to flow with decreasing f_l. The introduction of this momentum source influences the results of the simulation in two ways: 1) it will attenuate any bulk flow caused from the flow drivers present in the bulk liquid; and 2) it will attenuate the compensatory flow need to offset the volume change associated with solidification. As the formulation maintains mass continuity, this results in a pressure drop ΔP_d within the mushy zone - i.e. as f_l becomes smaller, the pressure differential needed to maintain continuity results in a pressure drop in the inter-dendritic liquid.

Eq [18] can be derived from the Darcy equation, which is routinely applied to solve for the velocity, or pressure drop, associated with flow through porous media. Assuming that the Carman-Kozeny equation[13] holds, A_{mush} is given by:

$$A_{mush} = \frac{180\mu}{\lambda_2^2} \quad \text{Eq [19]}$$

where λ_2 (μm) is the secondary dendrite arm spacing (SDAS). For the casting conditions used to produce aluminum alloy wheels, the average SDAS is approximately 40-50 μm. Assuming that the liquid viscosity is 0.0014 kg/m/s yields an A_{mush} around 10^8. A sensitivity analysis conducted with the model showed that the maximum pressure drop was highly dependent on the velocity attenuation parameter (A_{mush}), as would be expected. Due to the numerical convergence issues, the maximum value of A_{mush} had to be restricted to 10^7. As a result, it is likely that FLUENT™ will

underestimate the magnitude of pressure drop experienced due to flow attenuation toward the end of mass feeding and in areas of liquid encapsulation at low f_l.

Eq [3]

Solution Technique

The macroscale thermal-fluid-species model based on FLUENT^{TM} 16.0 was used to output the evolution in temperature, fraction liquid/solid, pressure and hydrogen concentration in the unit of mass fraction at points of interest in the wheel during solidification. This information was then input to the updated microporosity model, which is capable of predicting the bin-based, size distribution of hydrogen-based pores in A356. Using this approach, the nucleation and growth of pores in Stage I are tied to the local pressure, fraction liquid and concentration of hydrogen (accounting for macro-segregation associated with shrinkage-induced flow), in a sequentially coupled manner. *Note in stage II growth, pore growth is only tied to the evolution of fraction liquid*. A schematic of the overall modelling methodology and the flow of data is shown in Figure 4.

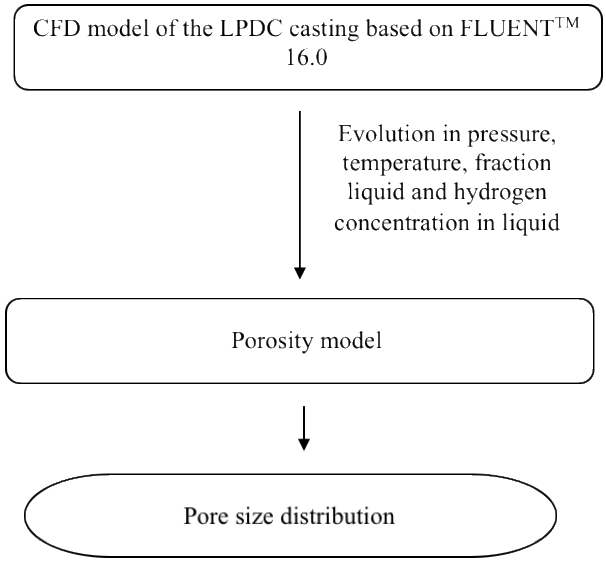

Figure 4 - Schematic of the overall modelling methodology used to predict pore size distribution for LDPC casting

The updated porosity model was written in Python (2.7). The new implementation was verified with the prediction from the previous implementation prior to updating the model. At each time step, once the local supersaturation becomes positive, the total number of pores are first

computed by integration of Eq [6] with respect to the local supersaturation. The pore radius is then updated through the either Eq [11] or Eq [17], depending on whether or not the local solid fraction at the current time step is in excess of the critical solid fraction, which has been assumed to be 0.9. The physical parameters in the model are listed in Table I.

Table I - Physical Parameters in the porosity model

	Value	Reference
Equilibrium constant in $[H] \Leftrightarrow \frac{1}{2} H_2$	$318.32 \times 10^{-\frac{2196}{T}-1.32}$	[13]
H diffusion coefficient in liquid, $D_{H,liq}$ (m^2/s)	$3.8 \times 10^{-6} e^{(-2315/T)}$	[4]
Density of liquid, ρ_l (kg/m^3)	2540	[3]
Surface tension of A356, γ (N/m)	0.79	[3]
H content cc/100 g Al (ppm)	0.15*	
Assumed initial pore radius (μm)	5	

*Typical value at the commercial facility

Results and Discussion

Porosity Modelling

Following XMT characterization, the pore size distribution estimated by the model was compared with the porosity data to provide validation. Locations 10T, 9B, 5BT, and 4B were identified as exhibiting the largest volume fraction of porosity of the locations examined via XMT and therefore were chosen for comparison to the model predictions for porosity. Figure 5 shows a contour plot of the hydrogen mass fraction distribution in the wheel cross-section near the end of solidification predicted by the FLUENT™ model. The locations that were analyzed with the porosity model are indicated by the black dots in Figure 5. The hydrogen concentrations predicted near the end of solidification at these locations are summarized in Table II. Based on the predictions of the segregation analysis, locations 9B and 5BT are enriched in hydrogen and locations 10T and 4B, were predicted to have approximately the same concentration as the initial liquid – i.e. no net macro-segregation.

Table II – Predicted Mass Fraction of Hydrogen at selected locations (*Note: initial bulk mass fraction hydrogen equal to 1.5×10^{-7}*)

Location	**Mass Fraction Hydrogen**
Location 10T	1.48×10^{-7}
Location 9B	1.75×10^{-7}
Location 4B	1.47×10^{-7}
Location 5BT	1.61×10^{-7}

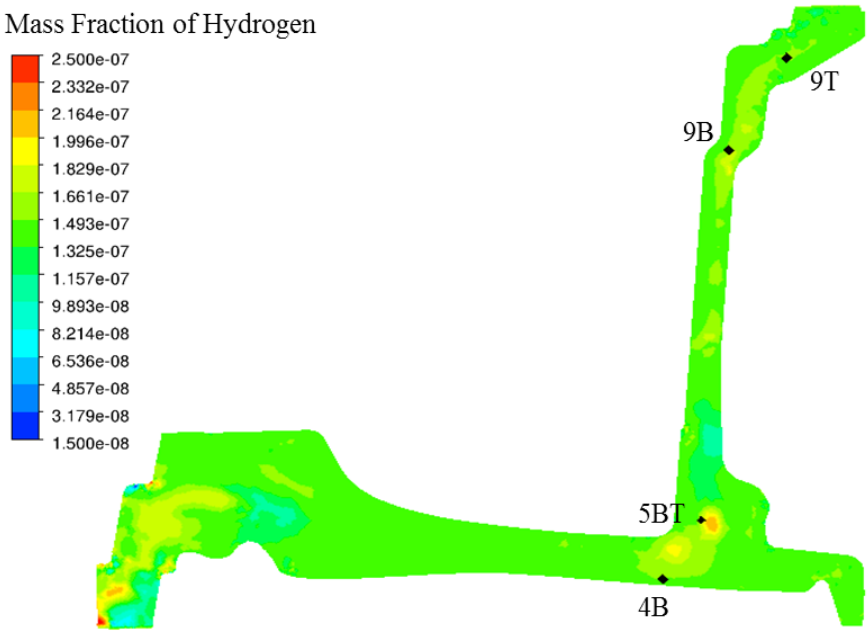

Figure 5 - Predicted hydrogen distribution in the wheel at the end of the casting process.

Nucleation Kinetics - A, ss_0 and σ estimation

The adjustable parameters *A*, ss_0 and σ in the equation describing the nucleation kinetics (Eq [6]) were determined by fitting with experimental data. Among the locations examined, location 9B is the best match to the conditions described by the original porosity model[9] – i.e. no liquid encapsulation – and therefore, the experimental data at location 9B was used to tune the adjustable parameters in the nucleation kinetics expression. A trial-and-error method was adopted to arrive at a set of nucleation parameters that gave the best fit for location 9B.

It is important to point out that the three parameters used to 'tune' the nucleation kinetics are likely to vary within the casting with the distribution of oxide-based nucleation sites [15]. Te set of three nucleation parameters has an effect on both the size range of the porosity that is predicated to form and the number of pores that are predicted to form. Additionally, these predictions are affected by the local cooling rate, local hydrogen content, and local pressure evolution. Of these, the cooling rate is validated independently against TC data extracted from the wheel and the macro-segregation of hydrogen has been indirectly validated based on Si macro-segregation [12]. The pressure evolution remains un-validated and is applied as estimated from the CFD model. The resulting dependence of size and number of pores on nultiple parameters, some of which have been independently validated, makes it relatively straightforward t arrive at a unique set parameter to describe the nucleation kinetics.

Figure 6 shows the difference in the expressions describing the nucleation kinetics between the original study[5], on which the porosity model was based, and the current work. The blue curve represents the nucleation site distribution used in Reference [5] while the red curve shows the nucleation site distribution used in the current study. The best fit to the experimental data at location 9B was achieved by assigning $A = 3\times10^{-9}$ m^{-3}, $ss_0 = 2.0$ mol/m^3 and $\sigma = 0.4$ mol/m^3. Based on the comparison in Figure 6, the number of nucleation sites activated as a function of hydrogen

supersaturation in the current work is lower than in the previous work. The lower number of nucleation sites may be related to differences in the liquid metal treatment in the commercial process in comparison to the previous laboratory-based study. In the commercial process, liquid metal is transferred to the die from the holding furnace through a transfer tube in which the entrance is located below the dross. Additionally, there is also a filter used at the top of the sprue. Both of these would reduce the number of oxide inclusions entering the die cavity and consequently the population of the nucleation sites available for pore nucleation[13]. The average hydrogen saturation ss_0 is also slightly increased from 1.7 to 2.0 mol/m^3 in the current work, indicating it is more difficult for a gas cavity to form on solid substrates. The reason for this difference is unclear and may be related to small variations in the alloy composition relative to the original study.

Having fit the porosity model to the experimental data from location 9B, the model was then used to predict the pore size distributions at locations 10T, 4B and 5BT using the same nucleation parameters.

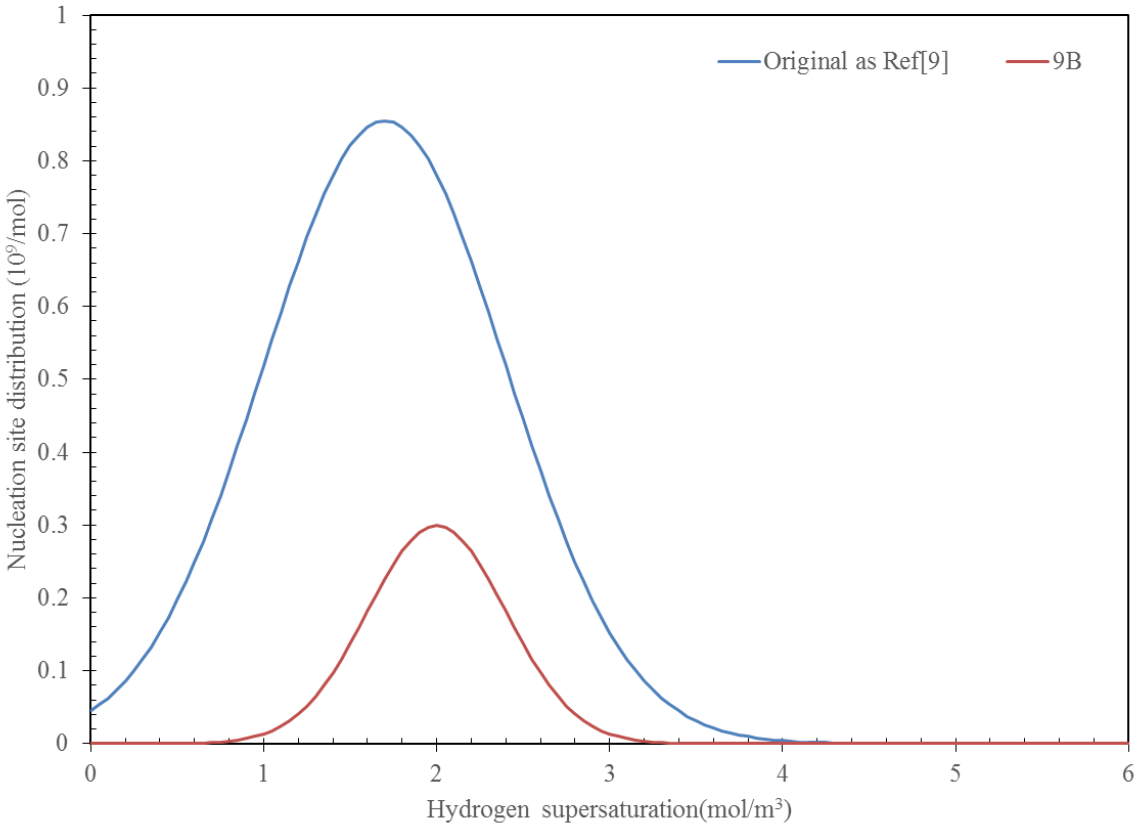

Figure 6 - Pore nucleation site distribution.

Figure 7(a) and (b) show the 3D rendering of the pores (LHS) and the corresponding predicted and measured pore size distributions (RHS), binned in 10-μm increments, at locations 4B, 10T, 9B and 5BT, with the critical solid fraction for mass feeding set to 0.9. As previously described, solidification with this particular die design begins approximately mid-rim and then proceeds simultaneously both up toward the in-board rim flange and down toward the rim/spoke

junction and then finally across the spoke, finishing at the top of the sprue. The two areas predicted to be prone to late-stage liquid encapsulation are in the upper in-board rim flange and at the rim/spoke junction, which is consistent with where the majority of porosity was found from the XMT analysis [12].

The measured data in Figures 7(a) and (b) are shown as the yellow bars and the predicted results as the red bars. The predicted cooling rate at each location was added to each plot for reference. Location 9B has an average cooling rate of 9.59 K/s; 10t, 3.7 K/s; 5BT, 1.45 K/s; and 4B 1.35 K/s. Overall, the results show good quantitative agreement in terms of the size distribution range at the various locations examined, apart from location 5BT. At location 5BT, the model over-predicted the porosity number density of large pores greater than 20-40μm; however, the amount predicted is negligible.

In contrast, there are significant errors in the estimate of the number density in at least some of the size ranges in all of the locations examined. Generally, however, the trend in number density within the size ranges predicted by the model is correct apart from at location 4B. At location 4B, the model significantly under predicts the number density of small pores (< 40 μm) in comparison to the XMT data. It is interesting to note that in the 3D rendered image at location 4B, there are clearly what appears to be a large number of tortuous pores in comparison to locations 9B and 10T. Thus, the discrepancy between the porosity predictions and the measurements at this location may be partially linked to the ability to resolve tortuous pores from the XMT data. While this may be a fair statement for the smaller pores measured at location 4B, it does not explain the general lack of quantitative agreement between the number density predicted by the model and the measurements—ie the error exceeds 100% in some locations. Currently, it is believed that the discrepancy is due to the variability in te population of nucleation sites. In the present approach, a single Gaussian-based population of nucleation sites is assumed to be applicable throughout the entire casting. It is possible that the population of nucleation sites, which is known to be influenced by the density of oxide inclusions, could vary throughout the casting [15]. At location 4B, another possibility for the discrepancy with the measurements is that during state II pore growth, at high f_s, as the local concentration of hydrogen becomes depleted, the pressure within the small pockets of liquid drops to below the vapour pressure of Al. This could potentially result in the cavitation of a large number of small Al-vapor bubbles (note: this would necessitate a different population of nucleation sites). Further work is needed to explore both possibilities.

Location 4B

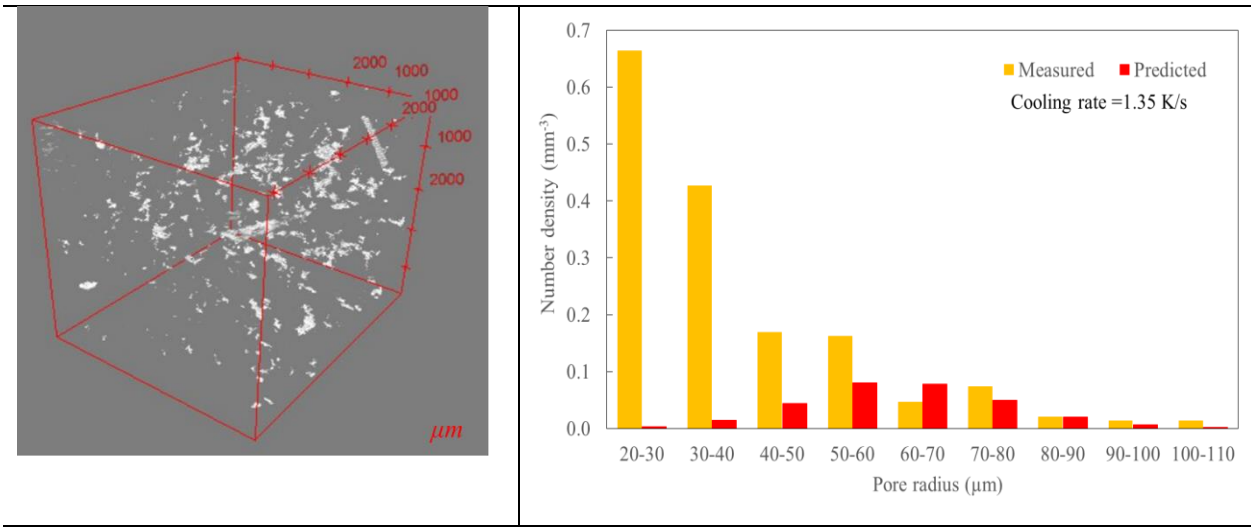

Location 9T

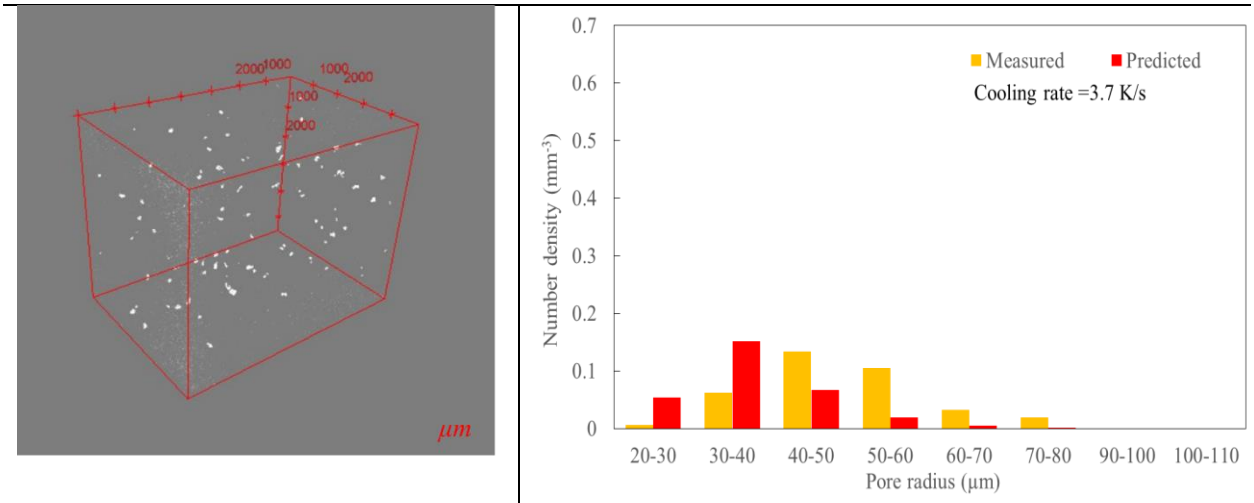

Figure 7 - 3-D characterization of porosity (Left) and comparison between measured and predicted pore size distribution (Right) at locations 4B, 9T.

Location 9B

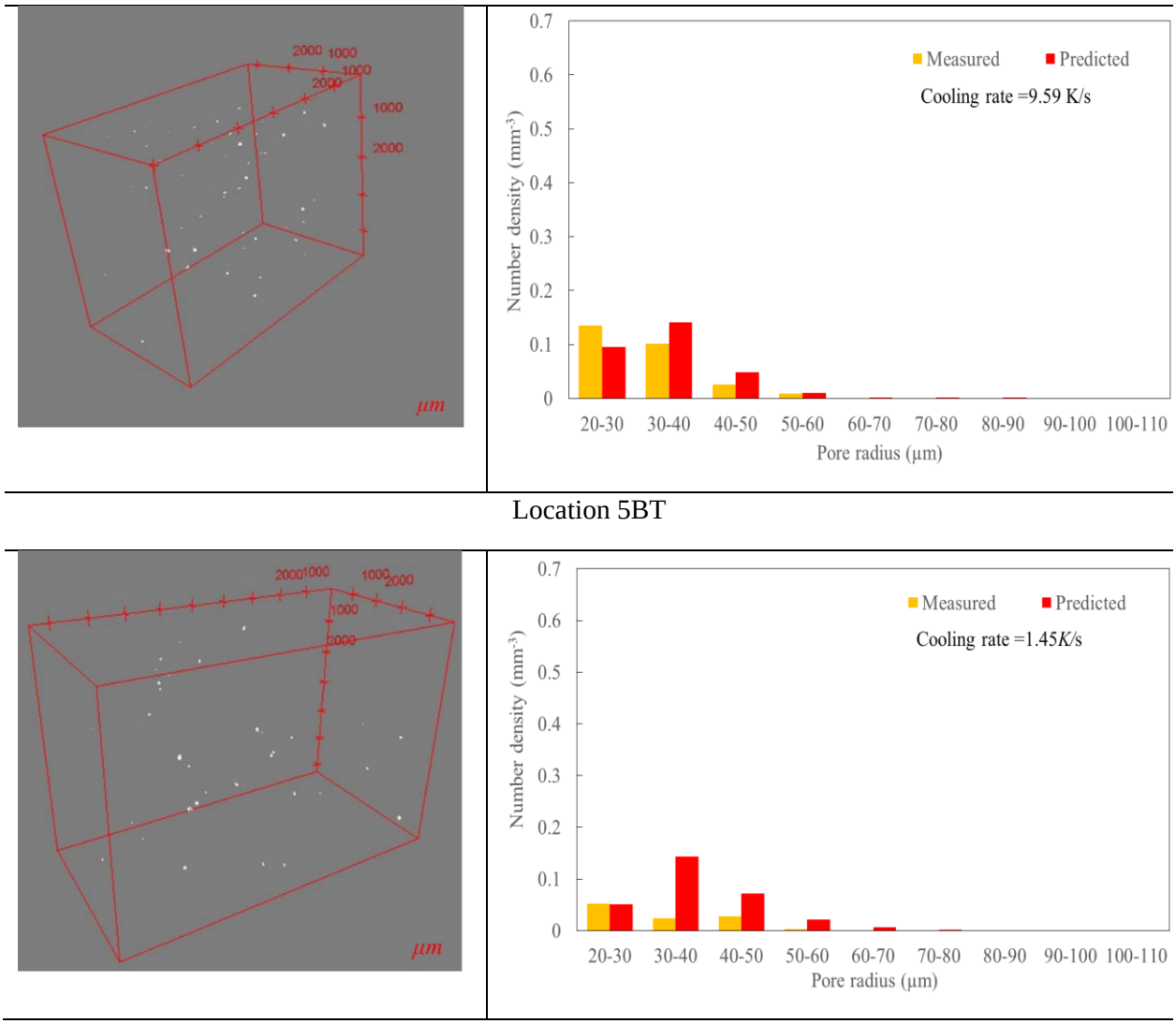

Figure 6 - 3-D characterization of porosity (Left) and comparison between measured and predicted pore size distribution (Right) at locations 9B, 5BT.

In terms of the model-predicted parameters, there are potentially three contributors to the evolution of pore size: 1) hydrogen segregation; 2) pressure drop; and 3) cooling rate. To explore the role of first two, the evolution in the liquid concentration of hydrogen and the evolution in the pressure have been plotted for the locations examined with the model. Figure 8 plots the variation in $C_{H,liq}$ with f_s and Figure 9 plots the variation in pressure with f_s.

Focusing first on the evolution of $C_{H,liq}$, the hydrogen concentration in the liquid increases with increasing f_s due to micro- and macro-segregation. The effect of macro-segregation is accounted for up to an f_s in the range of 0.45 to 0.55, which is where the eutectic phase transformation begins. Recall that species conservation is calculated in FLUENT^{TM} only up to the eutectic reaction. At f_s beyond the start of the eutectic transformation, the evolution in the liquid hydrogen concentration is driven solely by micro-segregation according to the Scheil approximation. The varying range in f_s arises due to silicon segregation, which impacts on the f_s at which the eutectic composition in the liquid is reached. Given the data shown, the evolution in

$C_{H,liq}$ with f_s is relatively consistent among the four locations examined with up to a ~25% difference between the location 5BT and 4B. At a given f_s, location 5BT generally exhibits the highest concentration of hydrogen in the liquid followed by location 4B, 9T and 9B, which is consistent with the contours of the predicted silicon segregation shown in previous work[10]. *Note the slight difference of species segregation arises from different partition coefficients.*

Based on the parameters in the nucleation kinetics expression, the average supersaturation (ss_0) for pore nucleation in the current model, is 2.0 (mol/m^3) and nucleation occurs over a range of supersaturation ($ss - ss_0$) from ~1.0 to ~3.0 (mol/m^3). This range has been added to Figure 8 for the limiting cases at locations 5BT and 9B for reference. It would appear that the majority of pore nucleation occurs at f_s's in the range of ~0.7 to 0.92 depending on the local enrichment of hydrogen, which is at relatively high solid fractions.

Figure 9 shows the local pressure evolution at the various locations examined. *Note: f_s corresponding to the eutectic phase transformation at each location is added for the reference.*There is an abrupt drop in pressure ΔP_d, ranging from approximately -18 to -24 kPa at each location. However, the range of solid fractions at which the pressure drop occurs varies from approximately 0.3 to 0.9, depending on location. Additionally, location 10T shows an increase in pressure after reaching the minimum at approximately 0.5 f_s, whereas the other three locations do not exhibit a pressure rise. Moreover, the pressure drop at locations 5BT and 9B occurs at f_s's approximately consistent with when the eutectic transformation occurs, whereas the pressure drop at locations 10T and 4B are very different – 10T occurring at an f_s of ~0.3 and 4B at an $f_s > 0.9$. The reason for the difference in behavior between the various locations is unclear. One hypothesis is that locations 10T and 4B are encouter some liquid encapsulation, where the pressure drop may be driven by the loss of feeding associated with encapsulation, whereas locations 9B and 5BT do not experience liquid encapsulation and therefore the pressure evolution may be more related to an abrupt change in the solidification rate associated with eutectic transformation.

Given the predicted differences in $C_{H,liq}$, ΔP_d and cooling rate occuring at the different locations of the wheel, it would appear that the evolution in pressure has the dominant effect on pore growth, but only under conditions where pores have nucleated prior to the pressure drop - i.e. at location 4B. Otherwise, the cooling rate appears to have the dominant effect, which explains why more porosity forms at location 9T compared to location 9B in spite of the pressure increase toward the end of solidification. Location 5BT is predicted to produce more porosity than locations 9T and 9B, because of the lower cooling rate and potentially also because of the slightly higher hydrogen content. A significant pressure drop predicted at 5BT occurs before pore nucleation and hence does not have a significant impact. The reason for the large discrepancy observed between the model predictions and XMT measurements at 4B with respect to small pores is still, however, not clear.

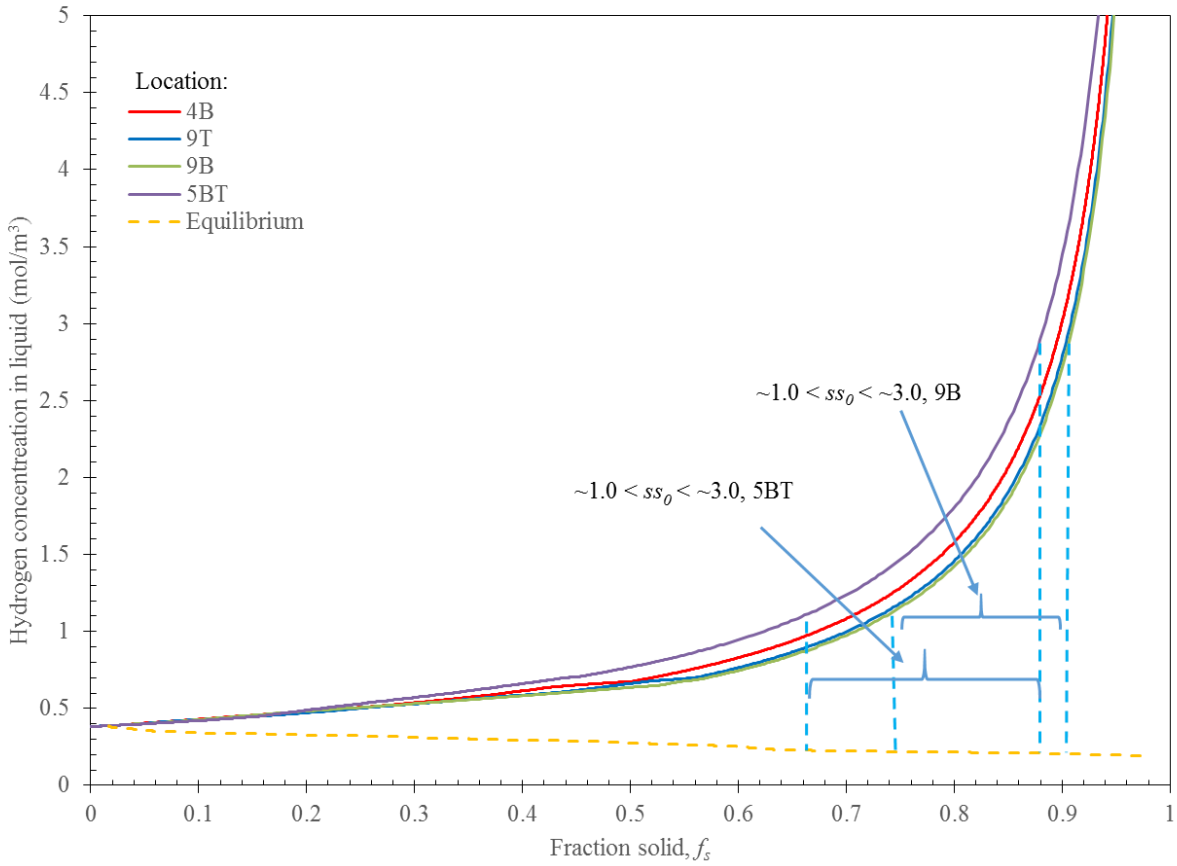

Figure 8 - Hydrogen concentration in liquid as a function of solid fraction at location 4B, 9T, 9B and 5BT.

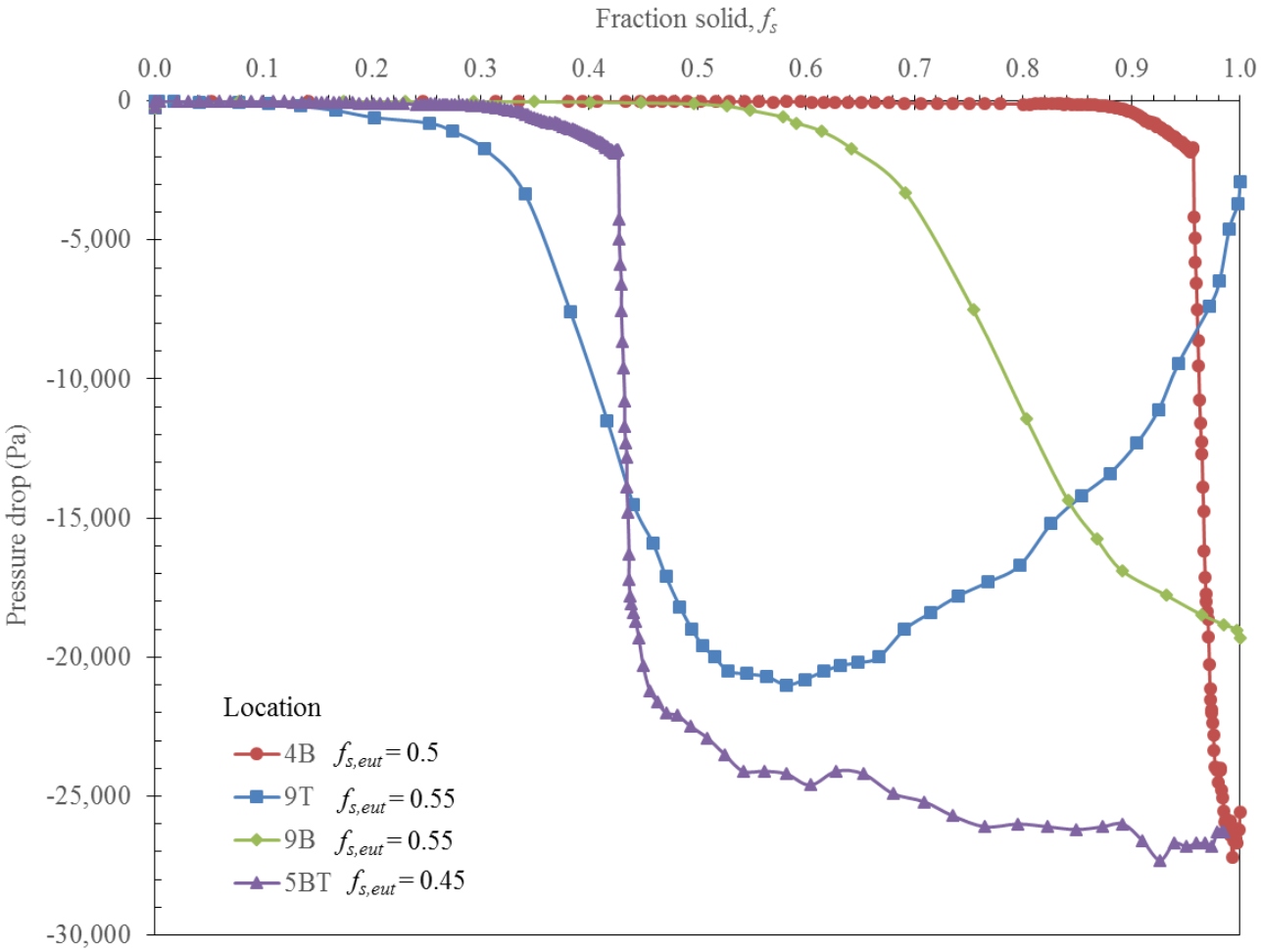

Figure 9 - Pressure drop as a function of solid fraction at location 4B, 9T, 9B and 5BT

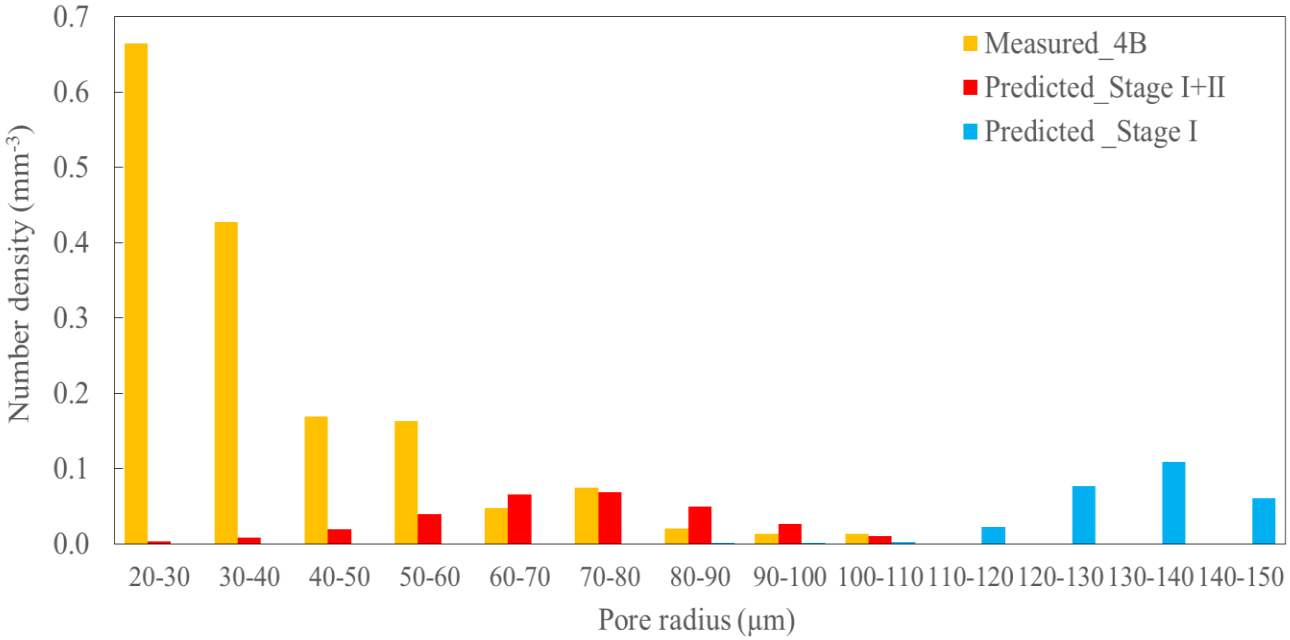

Figure 10 – Comparison between measured and predicted pore size distribution at location 4B adopting different growth mechanisms

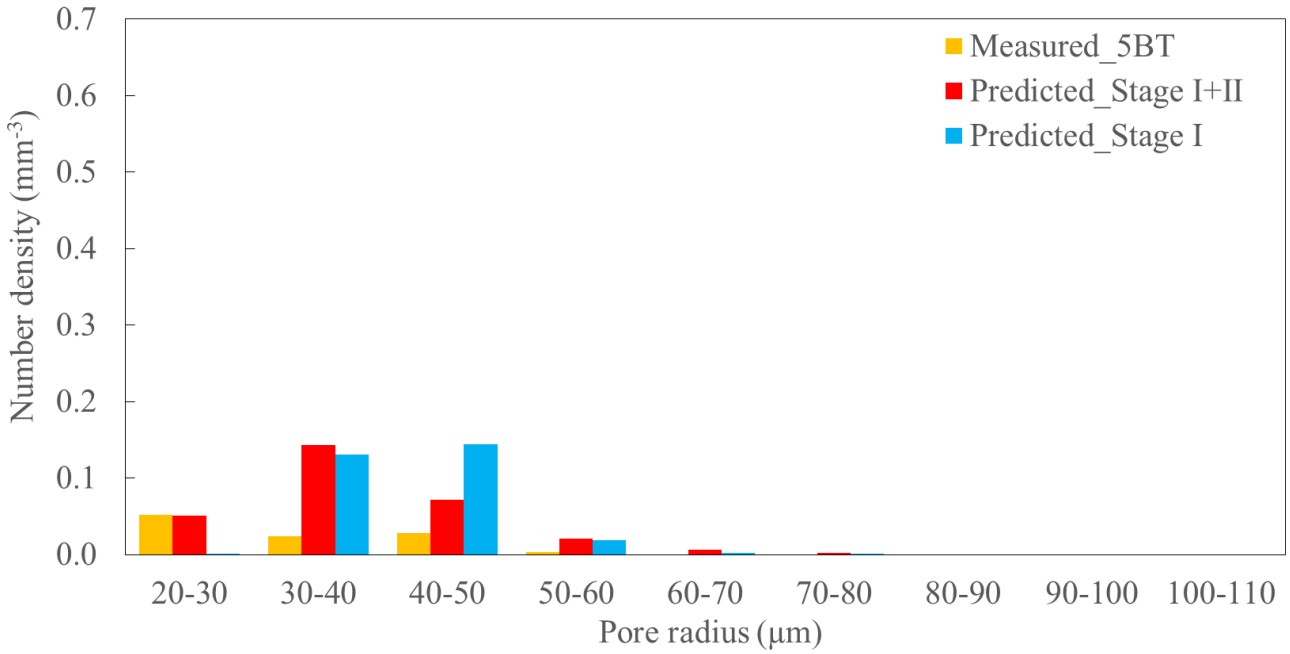

Figure 11 – Comparison between measured and predicted pore size distribution at location 5BT adopting different growth mechanisms

To assess the efficacy of the modifications made to the porosity model, an analysis was made in which the various modifications were sequentially switched on and the porosity distributions compared starting with the base model as previously described in Reference 5. Locations 4B and 5BT were chosen for the analysis. The resulting predicted pore size distributions, binned in 10 µm

increments, are shown in Figure 10 for location 4B and Figure 11 for location 5BT along with measure data (in yellow). The base model considering only stage I growth, without consideration of pressure drop and macro-segregation, is labeled stage I. Stage I with the addition of pressure drop is labeled Stage 1 + Pres; Stage I with the addition of pressure drop and segregation is labeled State I + Pres + Seg; and predictions with all of the modifications included is labeled Stage I + II + Pres + Seg.

The results indicate that the modifications made to the model generally imporved the prediction of the pore size distribtuion at 4B and 5BT. The effect of including all of the updates to the model is most dramatic at location 4B, where the prediction of the range in pore sizes is significantly improved with the elimination of the large pores. This is believed to be related to the fact that at location 4B there is a significant pressure drop during the late stages of solidification ($f_s > 0.9$) due to the loss of mass feeding leading to excessive pore growth. The two-stage approach limits late-stage growth at high f_s (refer to the effective colume in Eq. [15]). At location 5BT, the pressure drop occurs at an f_s around 0.45, consistent with eutectic transofrmation, therefore, before switching to the stage II growth approach. Hence, the improvement achieved with the modifications is less dramatic—*note: there is an imporvement in predicting porosity in the 20 to 30 μm range.* Another benefit of the two-stage approaches is that it is less reliant on an accurate prediction of the pressure drop at high f_s, which is difficult to achieve numerically.

Summary and Conclusions

A FLUENT^{TM} based thermal-fluid-solidification model augmented with a User-Defined-Subroutine (UDS) has been developed to predict hydrogen segregation, the evolution in hydrogen concentration in the liquid and the evolution in pressure in a commercially cast LPDC aluminum alloy wheel. Previous work has shown the model to be accurate in predicting the evolution in temperature and silicon segregation. The output from the FLUENT^{TM} based model including the evolution in temperature, f_l, composition of hydrogen in the liquid and pressure have been input to a standalone porosity model to predict the size distribution of porosity at discrete locations in the wheel. The standalone porosity model is based on previous work[5] and has been updated to include: 1) the evolution in hydrogen concentration in the liquid due to both macro-and micro-segregation; 2) the evolution in pressure; and 3) pore growth based on both diffusion and late-stage, inter-dendritic, pressure evolution. To provide data for validation of the pore model, XMT data were collected from samples taken from a cross section of the wheel and processed to yield the equivalent pore radius and the number density of pores. Four locations within the wheel were observed to have the highest amount of porosity and were compared with predictions obtained from the model.

The results of the model predictions for porosity show good agreement with XMT-based measurements in terms of the pore size range at the locations examined—specifically the upper rim and the rim/spoke junction. In contrast, the prediction of the number density of pores shows considerable error in all of the areas examined. In some of the size ranges, the error in number density exceeds 100%. Current thinking is that this large discrepancy between the model predictions for number density and the data dis due to the variability in the population of nucleation sites and that the single, Gaussian-based function used in the model may not be a good assumption—ie the population density may well vary with location in the casting. At location 4B, one of the locations close to the wheel/spoke junction, another possibility is that the pressure within the small pockets of isolated liquid that form at high f_s drops to below the vapor pressure of Al. This could potentially result in the cavitation of a large number of small Al-capor bubbles (note:

the formation of these pores could be associated with a different population of nucleation sites). Further work is needed to explore both possibilities.

The modifications to the pore model were shown to improve the predictive capabilities of the model when compared to the original formulation. In particular, the relatively accurate prediction of the pore size distribution leads the way to be able to predict spatial variability in the fatigue performance of the wheel. For the hydrogen content examined, the evolution in pressure (in particular the magnitude of ΔP_d) appears to have the dominant effect on pore growth, under conditions where pores have nucleated prior to an abrupt pressure drop. Otherwise, the cooling rate appears to have a significant role.

Acknowledgements

The authors gratefully acknowledge the financial support of the NSERC, under the Automotive Partnership Canada Program. ABP acknowledges use of the facilities and support provided by the Research Complex at Harwell, funded in part by the EPSRC (EP/I02249X/1 & EP/M009688/1).

References

[1] B. Zhang, S.L. Cockcroft, D.M. Maijer, J.D. Zhu, and A.B.Phillion:JOM, 2005, vol. 57, pp. 36–43.2.

[2] P.D. Lee, A. Chirazi, and D. See:J. Light Met., 2001, vol. 1,pp. 15–30.3.

[3] J.D. Zhu, S.L. Cockcroft, and D.M. Maijer:Metall. Mater. Trans.A, 2006, vol. 37A, pp. 1075–85.4.

[4] G. Backer and Q.G. Wang:Metall. Mater. Trans. B, 2007,vol. 38B, pp. 533–40.5.

[5] L. Yao, S. Cockcroft, J. Zhu, and C. Reilly:Metall. Mater. Trans.A, 2011, vol. 42A, pp. 4137–48.6.

[6] C. Puncreobutr, P.D. Lee, R.W. Hamilton, and A.B. Phillion:JOM, 2012, vol. 64, pp. 89–95.7.

[7] A. Bahmani, N. Hatami, and N. Varahram:Int J Adv ManufTechnol, 2013, vol. 64, pp. 1313–21.8.

[8] T. Wang, D. AN, Q. Zhang, and M. Zhu: inIOP Conf. Series:Materials Science and Engineering, 2015.9.

[9] V.R. Voller, A.D. Brent, and C. Prakash:Int. J. Heat MassTransf., 1989, vol. 32, pp. 1719–31.10.

[10] C. Beckermann:Int. Mater. Rev., 2002, vol. 47, pp. 243–61.11.

[11] M. Ghods, L. Johnson, M. Lauer, R.N. Grugel, S.N. Tewari, andD.R. Poirier:J. Cryst. Growth, 2016, vol. 449, pp. 134–47.12.

[12] P. Fan, S. Cockcroft, D. Maijer, L. Yao, C. Reilly, and A.Phillion:Metals (Basel), 2018, vol. 8, pp. 503–16.13.

[13] P.N. Anyalebechi:Scr. Metall. Mater., 1995, vol. 33, pp. 1209–16.14.

[14] K.D. Carlson, Z. Lin, and C. Beckermann:Metall. Mater. Trans.B, 2007, vol. 38B, pp. 541–55.15.

[15] L. Yao, S. Cockcroft, C. Reilly, and J. Zhu:Metall. Mater. Trans.A, 2011, vol. 43A, pp. 1004–16